Interface tailoring effect on magnetic properties and their utilization in MnGa-based perpendicular magnetic tunnel junctions

Q. L. Ma,[1,*] T. Kubota,[1] S. Mizukami,[1] X. M. Zhang,[1] H. Naganuma,[2] M. Oogane,[2]
Y. Ando,[2] and T. Miyazaki[1]

[1]*WPI Advanced Institute for Materials Research, Tohoku University, 2-1-1, Katahira, 980-8577 Sendai, Japan*
[2]*Department of Applied Physics, Graduate School of Engineering, Tohoku University, 6-6-05, Aoba-yama, 980-8579 Sendai, Japan*
(Received 20 February 2013; published 23 May 2013)

Insertion of a thin $3d$ ferromagnetic metal/alloy layer between the barrier layer and the perpendicularly magnetized ferromagnetic electrode is an effective method to enhance the magnetoresistance (MR) ratio in perpendicular magnetic tunnel junctions (p-MTJs). In the present paper we systematically studied the structural and magnetic properties as well as the spin-dependent transport in p-MTJs with a core structure MnGa/FM/MgO/CoFeB (FM = Fe, Co), with the MnGa being the $L1_0$ MnGa alloy ($Mn_{57}Ga_{43}$, $Mn_{62}Ga_{38}$) and the $D0_{22}$ MnGa alloy ($Mn_{70}Ga_{30}$). The insertion of the Fe and Co layers enhances the MR ratio significantly as well as the MnGa composition dependence of the MR ratio. In addition, opposite magnetic properties and $MR(H)$ curves of MTJs with Fe and Co interlayers are observed, naturally suggesting the ferromagnetic and antiferromagnetic exchange coupling for MnGa/Fe(bcc) and MnGa/Co(bcc), respectively. By considering the exchange coupling between the FM and MnGa, we successfully simulated the $MR(H)$ curves of the samples with Fe and Co interlayers based on a simple model. Furthermore, the interlayer effect on the transport properties are discussed based on the temperature dependence of the MR ratio by using the magnon excitation model modified with impurity-induced hopping. It shows that the FM interlayer restrains the impurity induced hopping and the magnon excitation; and furthermore, the Co is more effective in restraining the impurity diffusion and magnon excitation as compared to Fe.

I. INTRODUCTION

MnGa ordered alloys have drawn intensive attention because of the high perpendicular magnetic anisotropy (PMA), high spin polarization (P), low saturation magnetization (M_s), and low damping constant (α). Recent researches have shown that tetragonal $Mn_{3-\delta}Ga$ alloy exhibits a large PMA constant ($K_u \sim 10^7$ erg/cm^3) with a high Curie temperature of above 700 K.[1–4] In addition, Zhu *et al.* obtained a giant coercive force (H_c) of more than 4 T and a large magnetic energy product for the $L1_0$ ordered $Mn_{1.5}Ga$ alloy.[5] These properties make MnGa ordered alloy an excellent material for magnetic storage media because the high K_u allows for a small cell size of tens of nanometers with high thermal stability.[6,7] Mizukami *et al.* investigated the dynamic magnetic properties by using the time resolved magnetic optical Kerr effect (TRMOKE) technique and demonstrated a low damping constant (α) of about 0.01.[8] A high spin polarization (P) of more than 70% was predicted theoretically for MnGa alloys.[1,9,10] In 2011, Kurt *et al.* demonstrated on the basis of point contact Andreev reflection (PCAR) experiments where the values of P are 58% and 41% for Mn_3Ga and Mn_2Ga, respectively.[4,11] Besides, the magnetic properties of MnGa, such as M_s and H_c, can be easily tuned by controlling the stoichiometric composition. When the atomic composition changes from Mn poor to Mn rich, the magnetic order of the alloy changes from ferromagnetic to ferrimagnetic with decreasing M_s and increasing H_c.[3,9] These properties make the alloy an excellent candidate for spintronics applications as well, especially for Gbit spin transfer toque magnetic random access memory (STT-MRAM) applications.[6,7]

Several studies have been carried out on the MnGa bulk materials and thin films, including crystalline structural analysis, magnetic property investigation, magnetic dynamics, and spin-polarization measurement.[1–5,8–11] In contrast, the work on the spin-dependent tunneling (SDT) effect in MnGa alloys has hardly been investigated. Kubota *et al.* demonstrated the spin filter effect of MnGa on SDT by using MnGa as the spin polarizer in the MgO-based magnetic tunnel junction (MTJ).[12,13] However, the devices in this work are not fully perpendicular MTJs, and only a few percent of magnetoresistance (MR) ratio was obtained. In our previous work, fully perpendicular magnetic tunnel junctions (p-MTJs) based on the MnGa alloy were realized by using $L1_0$-$Mn_{62}Ga_{38}$ and perpendicularly magnetized CoFeB thin films.[14] However, the detailed magnetic and structural analysis was not performed. In p-MTJ materials, a thin $3d$ ferromagnetic metal and/or alloy (FM) layer with high spin polarization (such as Fe, Co, FeCo, or CoFeB) inserted between the perpendicularly magnetized ferromagnetic material (p-FM) and the barrier is a popular and effective method to improve the MR ratio.[15–17] As long as the coupling between the p-FM and the FM is strong enough to overcome the demagnetization effect of the FM layer, the magnetization switching of FM and p-FM by magnetic field is simultaneous. Thus, the hybridized ferromagnetic bilayer acts as single ferromagnetic layer. There have been many works on p-MTJs based Fe/Pt(Pd, Co) multilayer, $L1_0$-FePt alloy, and RE-TM alloys show that the MR ratio can be greatly enhanced by a $3d$ FM interlayer; and an MR of up to 100% has been reported for FePt/MgO/FePt p-MTJs with the CoFeB interlayer.[15–17] In those reports, the $3d$ metal insertion layer was demonstrated to be ferromagnetically coupled to the p-FM layer. However, the situation in a MnGa alloy is very complicated due to the magnetic coupling involved with a Mn atom is changeful, depending on the atomic distance and chemical environment.[18–20] The coupling between the p-FM

and the FM interlayer surely affects the SDT in MTJs with hybridized electrode structures, both on the spin filter effect and on the magnetic field response.[14,21]

Despite the progress that has been made on this material so far, as well as on SDT effect, detailed structural analysis of p-MTJs based on a MnGa/FM hybridized spin filter is lacking. Besides, the systematic MnGa composition dependence of the magnetic properties and SDT effect in these devices remain to be clarified. In the present work we systematically investigated the structural and magnetic properties of MnGa/FM stacks and their effect on the SDT in p-MTJs with cores structure of MnGa/FM/MgO/CoFeB. The FM layer here is typical $3d$ metal: Fe and Co. By controlling the MnGa composition, we fabricated p-MTJs based on the $L1_0$ MnGa alloy ($Mn_{57}Ga_{43}$, $Mn_{62}Ga_{38}$) and $D0_{22}$ MnGa alloy ($Mn_{70}Ga_{30}$). The rest of the paper is organized as follows. Section II introduces the experimental details, including the film deposition conditions, method for structural and magnetic property characterization, and the transport property measurement technique. Section III depicts the film stack structure and the interfacial properties based on x-ray diffractometry (XRD) and transmission electron microscopy (TEM). Section IV focuses on the magnetic properties of unpatterned MTJ films. Section V discusses the magnetoresistance effect of the p-MTJs. The MnGa alloy composition and the interlayer (Fe, Co) thickness dependence of the MR values are presented in this section. Furthermore, the *MR(H)* loops are discussed based on a simple model by taking into consideration the exchange coupling effect between MnGa and the FM interlayer. Section VI presents the temperature dependence of the MR ratio for p-MTJs with different FM thicknesses. The effect of the interlayer is discussed based on magnon excitation and impurity-assisted tunneling effect on the temperature dependence of the SDT.

II. EXPERIMENT

Film stacks were fabricated using an ultrahigh-vacuum sputtering system with a base pressure of less than 1×10^{-7} Pa. The core structure of the MTJ stacks was Cr(40)/MnGa(30)/FM(t_{FM})/Mg(0.4)/MgO(2.2)/CoFeB(1.2)/Ta(5)/Ru(7) (in nm), deposited on a MgO(001) single-crystal substrate. All the layers were deposited at room temperature, and an *in situ* annealing was carried out after the deposition of Cr and MnGa at 700 and 400 °C. For samples with Co as the interlayer, an additional *in situ* annealing was carried out after the deposition of Co and MgO at 350 and 300 °C for 30 and 20 min, respectively. The *in situ* annealing after the deposition of Co was necessary, because it enabled the Co interlayer to crystallize into bcc structure, which is the entailed structure for MgO-based MTJs to achieve high MR ratio. However, no *in situ* annealing is required in the case of Fe, because the bcc structure is a stable phase for Fe. Besides, avoiding *in situ* annealing is a benefit to restraining the element diffusion. The *in situ* annealing temperatures and durations for the samples with Fe and Co interlayers are provided in Table I. The thickness of the Fe interlayer is varied as $t_{Fe} = 0, 0.8, 1.1$, and 1.5 nm. The thickness of the Co interlayer is varied as $t_{Co} = 0, 0.8, 1.0$, and 1.5 nm. The interlayers are limited to a thickness of 1.5 nm to maintain the PMA. MnGa ordered alloy films on the Cr buffer layer as well

TABLE I. *In situ* annealing temperatures after the deposition of each layer for different series of samples.

	Series I (Fe interlayer)	Series II (Co interlayer)
Cr	700 °C (1 h)	700 °C (1 h)
MnGa	400 °C (1 h)	400 °C (1 h)
FM	–	350 °C (0.5 h)
MgO	–	300 °C (20 min)

as thin CoFeB films on the MgO barrier layer exhibit high PMA as we already demonstrated.[3,22] After stack deposition, the films were patterned into junctions with sizes range from $10 \times 10 \ \mu m^2$ to $100 \times 100 \ \mu m^2$ using typical UV lithography combined with Ar etching.[13,22] All the junctions were then annealed for 1 h with a magnetic field of 1 T applied perpendicular to the film in order to crystallize the CoFeB electrode. The post-annealing temperature for series I and series II are 275 and 300 °C, respectively.

The composition of the MnGa alloy was analyzed by inductively coupled plasma (ICP) mass spectrometry. Crystal structure characterization of the MnGa electrodes in the MTJ structure was performed using typical out-of-plane XRD with 9-kW rotating anode. The Cu K_α line (wave length $\lambda = 1.5418$ Å) was used in the experiment. Two-dimensional XRD in the 2θ-χ plane was also performed to check the single crystalline quality and the lattice orientation of the films. To examine the interfacial properties of the MnGa/FM/MgO structure as well as the crystalline quality of the top CoFeB electrodes, the TEM measurements were carried out on the samples with $Mn_{62}Ga_{38}$/Co as the electrode. The magnetic properties were measured by using a vibrating sample magnetometer (VSM) at room temperature with a range of -2 to 2 T. The transport properties, including MR effect and the temperature dependence of the resistance, were tested using a physical property measurement system (PPMS) by the typical four-probe method.

III. MTJ STACK STRUCTURE CHARACTERIZATION

The XRD analysis of the samples with a 1.5 nm Fe(Co) interlayer are shown in Fig. 1. The out-of-plane 2θ XRD pattern of MnGa(30 nm)/FM(1.5 nm) (FM = Fe, Co) are shown in Figs. 1(a), 1(b), and 1(c). The (002) and (004) peaks of the MnGa electrode are clearly seen in each pattern, and the other peaks correspond to the substrate. The (002) and (004) peaks are attributed to the superlattice of $L1_0$ ordering and the fundamental peaks of $L1_0$ and $D0_{22}$ MnGa alloys for the unit cells. The (002) peak positions of $Mn_{57}Ga_{43}$, $Mn_{62}Ga_{38}$, and $Mn_{70}Ga_{30}$ are located at 24.5°, 24.5°, and 25.1°, respectively. The corresponding out-of-plane lattice constant c for $Mn_{57}Ga_{43}$ and $Mn_{62}Ga_{38}$ is 7.26 Å ($2c$) with $L1_0$ structure, while it is 7.09 Å for $Mn_{70}Ga_{30}$ with the $D0_{22}$ structure. These results are consistent with those for single MnGa films deposited on a Cr buffer layer.[2,3] In our samples, the position and half-width of the peaks are independent of the interlayer material and its thickness. This indicates that the effect of the interlayer on the structure of the MnGa layer is negligible, because the MnGa thickness is much larger than the
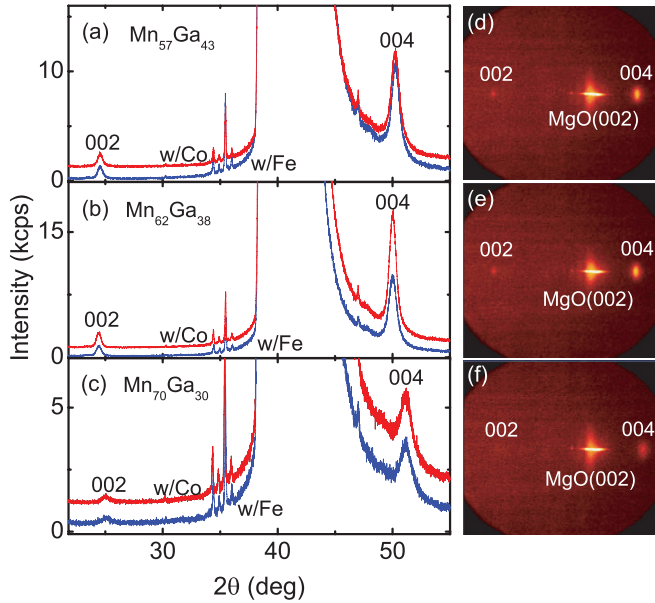
FIG. 1. (Color online) Out-of-plane XRD patterns of p-MTJs with a 1.5 nm Fe and Co interlayer. (a), (b), and (c) The $Mn_{57}Ga_{43}$, $Mn_{62}Ga_{38}$, and $Mn_{70}Ga_{30}$ samples. (d), (e), and (f) The 2D XRD patterns in the 2θ-χ plane for the samples with the Fe as interlayer.

interlayer thickness. To further check the (001) orientation of the MnGa electrodes, two-dimensional XRD was performed in the 2θ-χ plane. The results for the samples with 1.5 nm Fe interlayer are shown in Figs. 1(d), 1(e), and 1(f) for different MnGa compositions. The MnGa (002) and (004) diffractions are indicated by a dot along the $\chi = 0$ line, which reflect the highly (001) oriented structure of the MnGa layer. This was also confirmed by the TEM image.
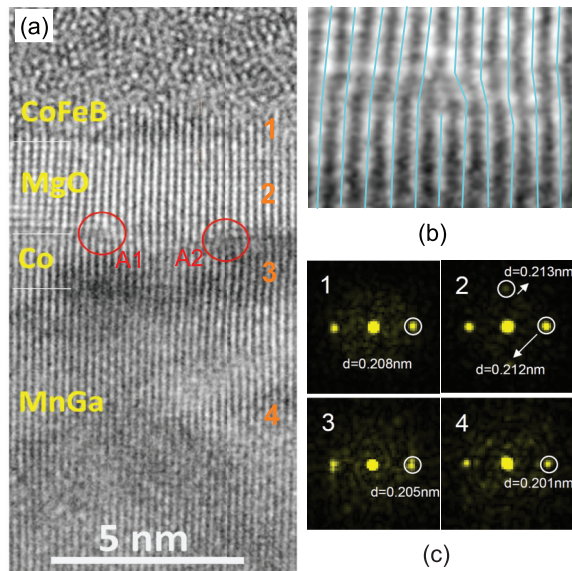

FIG. 2. (Color online) TEM images of the sample with the stack structure $Cr(40)/Mn_{62}Ga_{38}(30)/Co(1.5)/MgO(2.2)/CoFeB(1.2)/Ta(5)/Ru(7)$ (in nm). (a) Cross section TEM image. (b) Detailed atomic structure of area A1 in (a). (c) FFT pattern of the area marked by 1, 2, 3, and 4 in (a).

Figure 2 shows the TEM images of the sample with the structure $Cr(40)/Mn_{62}Ga_{38}(30)/Co(1.5)/MgO(2.2)/CoFeB(1.2)/Ta(5)/Ru(7)$ (in nm). The post-annealing condition of the sample used for the TEM measurement is the same as that for the MTJ samples used for transport property investigation. As shown in the cross section TEM image [Fig. 2(a)], the MnGa layer and MgO barrier have a well crystallized epitaxial structure, and the Co layer crystallized as a template of MnGa due to the *in situ* annealing after Co deposition. Because of the thin thickness and the low post-annealing temperature, the top CoFeB layer is partially crystallized. Another apparent characterization is the presence of dislocations (marked with A1 and A2) at the Co/MgO interface. The detailed structure of the dislocation A1 is shown in Fig. 2(b), and it is found to be a typical edge dislocation. The in-plane lattice constant of Co depends on the MnGa layer, while the lattice constant of MgO is about 7.5% larger than that of MnGa; hence, the formation of dislocations serves to reduce the stress resulting from the lattice mismatch. The similar phenomenon was also observed in epitaxial Fe/MgO/Fe MTJs, and it has been shown that the disorder reduces the MR ratio.[23] Figure 2(c) shows the FFT fitted pattern of positions 1, 2, 3, and 4. The fitted pattern shows a similar large lattice mismatch between MnGa and the MgO barrier layer, and Co is likely have a bcc structure with an epitaxial relationship of Co(001)[110]‖MnGa(001)[100]. This result is consistent with the case in τ-MnAl/Co, as reported by Lauhoff *et al.*[18]

IV. MAGNETIC PROPERTIES

Figure 3 shows the magnetization per area as a function of applied magnetic field [$M/A(H)$ loops] of the continuous film of the MTJ stacks. Figures 3(a), 3(b), and 3(c) show the loops of the samples with and without Fe insertion, in the case of the $Mn_{55}Ga_{45}$, $Mn_{62}Ga_{38}$, and $Mn_{70}Ga_{30}$ electrodes, respectively. For the three different MnGa electrodes, the $M(H)$ curves with Fe insertion show a larger magnetization and a relatively smaller H_c. The remanent magnetization increases and the H_c decreases which originate from the ferromagnetic coupling between the Fe interlayer and the MnGa layer. The small step around zero field is the signal from the CoFeB top electrode. The remanent magnetization per unit area (M_r/A) of the samples is summarized in Fig. 3(d). M_r/A of MnGa/Fe shows a linear monotonic increase with t_{Fe}, indicating that the Fe layer exhibits a well PMA of up to 1.5 nm. The slope of the increase [$\Delta(M_r/A)/\Delta t_{Fe}$] is almost the same, as shown with the dashed lines for the three different MnGa compositions.

The effect of the Co interlayer is opposite, as shown in Figs. 3(d)–3(g). The $M/A(H)$ curves of samples with the Co interlayer show a smaller magnetization and a relatively larger H_c. The decrease in the magnetization suggests an antiferromagnetic (AF) coupling between MnGa and the Co layer.[14,18] The spin-flopping structure at the MnGa/Co interface due to the AF coupling could be the reason for the enhanced H_c of the MnGa/Co bilayer.[24] The M_r/A values of MnGa/Co as a function of the Co thickness are summarized in Fig. 3(h). It shows a linear decrease with t_{Co}. The slope of the increase [$\Delta(M_r/A)/\Delta t_{Co}$] is around 2300 emu/cm^3 for the three different MnGa compositions, and this value is similar to that for the Fe interlayer. The large slops may be derived
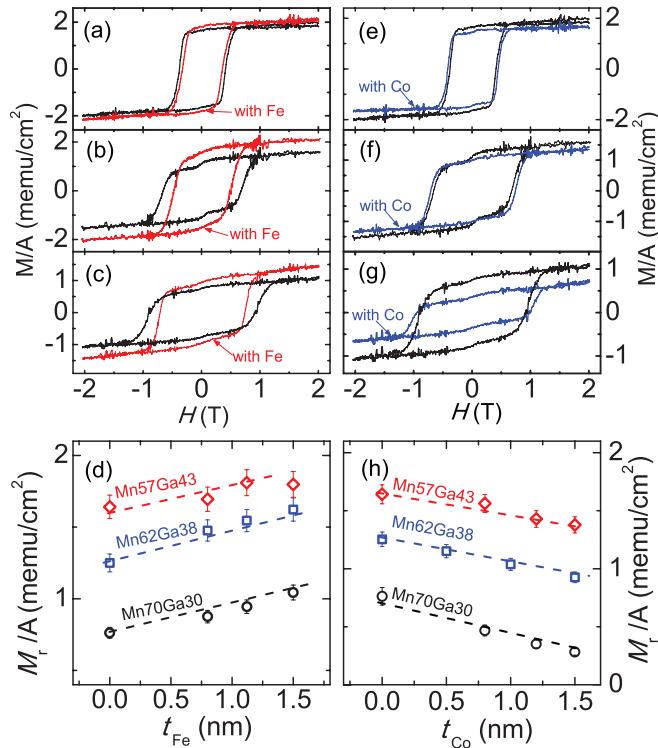
FIG. 3. (Color online) *M/A(H)* loops of p-MTJs with/without the 1.5 nm Fe (Co) interlayer are shown in (a), (b), and (c) [(e), (f) and (g)]. (a) and (e), (b) and (f), and (c) and (g) The results for the samples with $Mn_{57}Ga_{43}$, $Mn_{62}Ga_{38}$, and $Mn_{70}Ga_{30}$ electrodes, respectively. The values of M_r/A for series I (Fe interlayer) and series II (Co interlayer) are summarized in (d) and (h).

from the interfacial enhancement of the magnetization as well as the interdiffusion at the MnGa/Co interface.

The situation of MnGa/FM interface is complicated due to the uncontrolled interdiffusion which coexists with the ideal clear interface. There may be MnGaFe or MnGaCo formed near the interface, because both MnGaCo and MnGaFe are thermally stable structures. In our experiment, the magnetic properties of MnGa/FM are similar for different MnGa alloy compositions, and the slopes $[\Delta(M_r/A)/\Delta t_{FM}]$ too are the same for all three compositions. If there is strong interdiffusion at the interface and MnGa-FM alloy is formed, the magnetic properties would be different for different MnGa compositions, as the atomic ratio is different. However, since the magnetic properties of MnGa/FM are similar as shown in Figs. 3(d) and 3(h), this possibility is ruled out. Thus, it is reasonable to consider the MnGa/FM clear interface to be the dominant one in our samples.

V. SPIN-DEPENDENT TUNNELING

A. Magnetoresistance effect

MR(H), calculated by the formula $(R_H - R_P)/R_P \times 100\%$, as a function of the applied field for samples with a 1.5 nm Fe and Co interlayer, for the $Mn_{62}Ga_{38}$ electrode, is shown in Figs. 4(a) and 4(b). The MR ratio defined as $(R_{AP} - R_P)/R_P \times 100\%$, for samples with 1.5 nm Fe and Co interlayers is 51% and 40%, respectively. $R_{P,AP}$ represents the parallel and
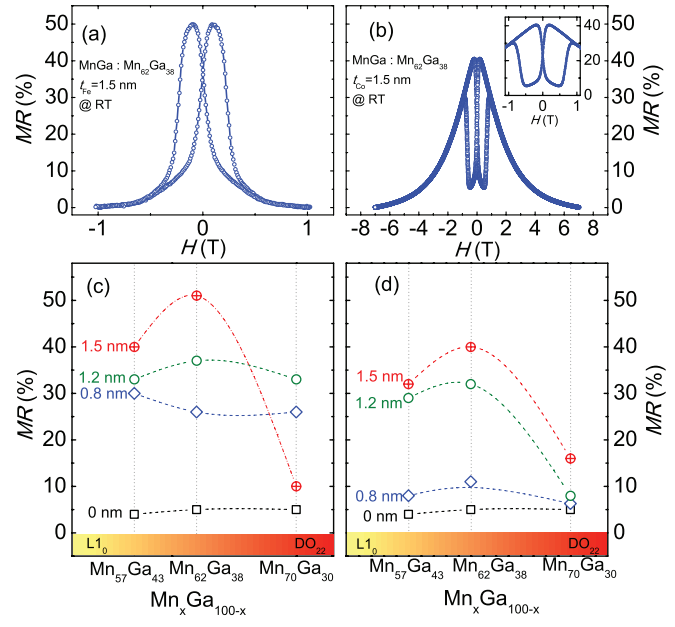

FIG. 4. (Color online) (a) and (b) The room temperature *MR(H)* loops for samples with the core structure $Mn_{62}Ga_{38}(30)/Fe(1.5)/MgO(2.2)/CoFeB(1.2)$ and $Mn_{62}Ga_{38}(30)/Co(1.5)/MgO(2.2)/CoFeB(1.2)$ (in nm). (c) and (d) The MR ratio at room temperature as a function of MnGa composition and the thickness of Fe and Co interlayers.

antiparallel magnetization configurations of the ferromagnetic layers in contact with the MgO barrier, and R_H represents the resistance values of a certain field strength (H). The MTJs with the Fe interlayer show an typical pseudospin valve type *MR(H)* curve. For junctions with the Co interlayer, a completely different *MR(H)* curve is observed. In the low field range, it shows a inverselike curve, as seen in the inset of Fig. 4(b). Four low-resistance states are seen in one full loop, independent of the MnGa composition. By taking into consideration the antiferromagnetic coupling between the Co and the MnGa layer, the *MR(H)* curve can be well explained (see Sec. V B).

Although the shape of the *MR(H)* curve for samples with Fe and Co interlayers are different, a significant enhancement of the MR ratio is seen in both cases. The MR ratio as a function of the interlayer thickness and MnGa composition are plotted in Figs. 4(c) and 4(d) for the the Fe and Co interlayers, respectively. As the interlayer thickness increases, the SDT in MTJs is gradually dominated by the Fe or Co layer, and hence, the MR ratio is enhanced. In MnGa/MgO based MTJs, the interfacial electronic state, the large mismatch between the MnGa and MgO layers, and the Mn atoms possibly diffused into the barrier, are all cause for the decrease of the MR ratio.[12–14] This is probably the reason for the low MR ratio of about 5% in MnGa/MgO based MTJs without FM interlayer.

Furthermore, in the samples with a Fe or Co interlayer, the MR ratio show an obvious dependence on the MnGa composition. Generally, there are two factors affecting the MR ratio in our p-MTJs when a thin FM layer is introduced between the MnGa layer and the barrier layer. One is the exchange coupling strength (J_{ex}); a large J_{ex} helps maintain the PMA of the FM interlayer, which is advantageous for MR enhancement. The other factor is the diffusion of Mn
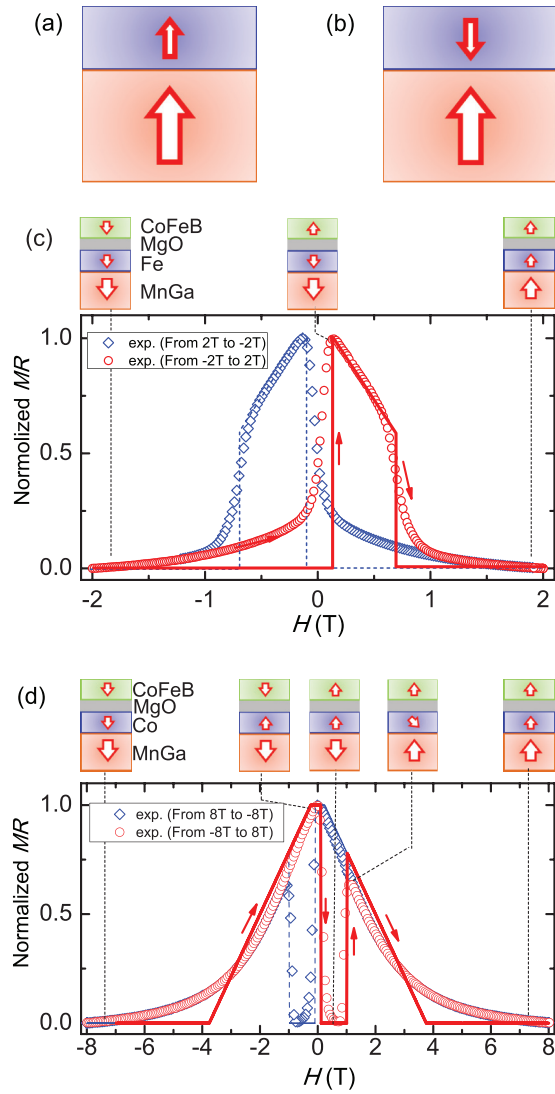
FIG. 5. (Color online) Two types of the coupling between p-FM and FM interlayer, ferromagnetic (a) and antiferromagnetic (b), for Fe/MnGa and Co/MnGa. (c) and (d) The normalized $MR(H)$ loops for series I and series II. The experimental data are marked by open dots, while the fitting is shown by solid lines. Red open circles show the data for the field sweep from negative to positive, and the blue diamonds show the opposite case. The magnetization process for the field sweep from negative to positive is shown at the top of each figure. The experiment data in (c) and (d) are for the samples with 1.1 nm Fe and 1.0 nm Co, with $Mn_{62}Ga_{38}$ as the electrode, tested at 5 K.

atoms from the MnGa layer. The Mn-rich MnGa alloy causes relatively stronger Mn diffusion and enhances the spin-flip process, which in turn negatively affects the MR ratio. The maximum MR ratio are obtained for the samples with $Mn_{62}Ga_{38}$, both with Fe and Co interlayers, probably due to the balance between the two above-mentioned factors.

B. Origin of the shape of $MR(H)$ loops

The increase in $(M_{r(MnGa/Fe)}/A)(t_{Fe})$ and decrease in $(M_{r(MnGa/Co)}/A)(t_{Co})$ naturally suggest the ferromagnetic and antiferromagnetic coupling for MnGa/Fe and MnGa/Co as

shown in Figs. 5(a) and 5(b), respectively. The exchange coupling type is directly related to the $MR(H)$ curve. In this section we discuss the exchange coupling effect on the shape of the $MR(H)$ curve.

The $MR(H)$ can be deduced based on a simple model, in which the relative MR ratio is dependent on the angle between the direction of magnetizations of the two ferromagnetic layers in contact with the MgO barrier.

$MR(H) \propto 1 - \cos\theta$, where θ is the relative angle between the direction of magnetization of the bottom ferromagnetic electrode and the top ferromagnetic electrode under a certain applied field.

The bottom electrode here is MnGa, Fe, and Co for samples without the interlayer, with the Fe interlayer, and with the Co interlayer, respectively. The top electrode is the CoFeB layer.

The angle θ can be decided on the basis of the free energy of magnetization for the MnGa/FM bilayer by taking into consideration the exchange coupling and the applied field. Considering $t_{MnGa} \gg t_{FM}$, we neglect the influence of the FM on the MnGa layer and consider that the switching of the MnGa layer only depends on the applied field. Thus, the FM magnetization direction is determined only by the energy minimum condition for the magnetization of the FM layer, which is described by following equation: $E_{FM} = t_{FM}(-M_{FM}H\cos\vartheta_{FM} - K_{FM}\cos^2\vartheta_{FM}) - J_{ex}\cos(\vartheta_{MnGa} - \vartheta_{FM})$. t_{FM} and M_{FM} are the thickness and saturation magnetization of the FM interlayer, respectively. ϑ_{FM} is the angle between the FM magnetization and the field direction. ϑ_{MnGa} is the angle between the MnGa magnetization and the field direction. J_{ex} represents the exchange coupling strength, which is positive for MnGa/Fe and negative for MnGa/Co. In the simulation, the magnetization are taken as 1200 and 1600 emu/cc for Co and Fe, respectively.[25]

The typical simulated $MR(H)$ curves for samples with a 1.1 nm Fe and a 1.0 nm Co interlayer are shown in Figs. 5(c) and 5(d), respectively. The related experimental data are also shown in the figure by open dots. The simulated curve and experimental data fit well in general. For this fitting we use the macrospin to describe the magnetization of the FM layer. However, nonuniform rotation of the FM magnetization might exist, and this probably is the reason for the large discrepancy between the experimental data and simulated curve at around 4 T. By comparing the simulated curve and experimental data, the coupling strength can be estimated. The coupling strength of $L1_0$-MnGa/Co ($D0_{22}$-MnGa/Co) and $L1_0$-MnGa/Fe ($D0_{22}$-MnGa/Fe) is estimated about -3.5 (-5) and 2.0 (3.0) erg/cm^2, respectively. To further understand the detailed magnetization process and spin structure in the coupled structure, a micromagnetic method needs to be adopted.

VI. TEMPERATURE DEPENDENCE OF SPIN-DEPENDENT TUNNELING

As the temperature decreases, the MR ratio increases depending on the electrode/barrier material and the MTJ stack structure. The temperature dependence of the MR ratio is closely related to the spin-dependent electron transport mechanism. Several studies have focused on the temperature dependence of the MR ratios in in-plane magnetized MTJs

including AlO-based MTJs and MgO-based MTJs.[26–31] In MgO-based MTJs, as demonstrated by Drewello *et al.* and Bond *et al.*, magnon excitation plays an important role in spin-dependent transport and accounts for the temperature dependence of the MR ratio. The model based on magnon assisted electron inelastic tunneling has been used to explain the temperature dependence of the MR ratio in various types of MTJs.[32–35] In this scenario, the magnon assisted tunneling opens an additional transport channel, which allows for electron transport between the spin-down and spin-up bands via the spin-flip process. This additional conductance channel decreases the spin filter effect in MTJs. As the temperature decreases, the contribution of magnon assisted tunneling decreases, thus causing the MR ratio to increase as the temperature decreases. Since this model is based on magnon excitation on the surface of ferromagnetic electrode in contacted with the barrier, it is also suitable for studying the MTJs based on hybridized electrodes, as in our case.

In this model, the conductances of the P and AP configurations are described as follows[32,33]:

$$G_P(T,0) = G_P(0,0)\left[1 + Q\xi\frac{2S}{E_m}k_B T\ln\left(\frac{k_B T}{E_c}\right)\right], \quad (1)$$

$$G_{AP}(T,0) = G_{AP}(0,0)\left[1 + Q\frac{1}{\xi}\frac{2S}{E_m}k_B T\ln\left(\frac{k_B T}{E_c}\right)\right], \quad (2)$$

where $G_{P,AP}(0,0)$ is the conductance in the parallel and antiparallel state at zero temperature ($T = 0$) and zero bias voltage. The parameter Q describes the probability of involvement of a magnon in the tunneling process. S is the spin number, while E_m is related to the Curie temperature [$E_m = 3k_B T_C/(S+1)$] of the ferromagnetic electrode. The parameter ξ is the ratio of the products of the density of state in the parallel and antiparallel configurations: $\xi = 2\rho_M\rho_m/(\rho_M^2 + \rho_m^2)$, which is approximated as $G_{AP}(0,0)/G_P(0,0)$. E_c is the magnon cutoff energy, which is a fitting parameter that depends on the structure and material of the ferromagnetic electrode.

The thermal smearing effect on the electronic structure of FM electrodes is estimated by

$$\frac{G(T,0)}{G(0,0)} = \frac{CT}{\sin(CT)}, \quad (3)$$

with $C = 1.387 \times 10^{-4}d/\sqrt{\phi}$, where d and ϕ are the barrier thickness (unit in Å) and height (unit in eV). The MgO barrier thickness of our junction is 2.2 nm for all the samples. Taking the barrier height of $\phi = 3.5$ eV as in Ref. 33, the calculated C value is 1.79×10^{-3}.

Element diffusion is inevitable during sample annealing when MnGa is used as the electrode because of the diffusion of the Mn atoms.[28,33,36] In particular, for the samples with a thin FM interlayer ($t_{FM} \leqslant 0.8$ nm), a strong temperature-dependent resistance is seen both in the P and AP configurations, which is evidence of the impurity assisted hopping, as demonstrated by Lu *et al.* for MgO based MTJs.[27] For one-step hopping in MTJs with a thin MgO barrier, the hopping conductance is described by $\sigma T^{1.33}$.[26–28] σ here denotes the probability of involvement of the hopping process in the total conductance, which is a fitting parameter. By taking into consideration this

contribution, the temperature dependence of the transport thus is formulated as follows:

$$G_P(T,0) = G_P(0,0)\frac{CT}{\sin(CT)}$$
$$\times \left[1 + Q\xi\frac{2S}{E_m}k_B T\ln\left(\frac{k_B T}{E_c}\right)\right] + \sigma T^{1.33}, \quad (4)$$

$$G_{AP}(T,0) = G_{AP}(0,0)\frac{CT}{\sin(CT)}$$
$$\times \left[1 + Q\frac{1}{\xi}\frac{2S}{E_m}k_B T\ln\left(\frac{k_B T}{E_c}\right)\right] + \sigma T^{1.33}. \quad (5)$$

In our samples, the temperature dependence of the MR ratio varies as the MnGa composition and interlayer thickness change. Three cases can be identified in our samples, depending on the FM layer material and thickness. The samples without the interlayer and that with a thin interlayer show a strong temperature dependence of both R_P and R_{AP}, and the MR ratio increases by more than 3 times as the temperature decreases from 300 to 5 K (case i). When an appropriate FM is introduced between MnGa and the MgO barrier, the temperature dependence of the transport becomes similar to that for typical MgO-based MTJs, in which MR(5 K) (MR ratio at 5 K) is twice MR(300 K), and R_P is nearly independent of temperature (case ii). The other case, as the FM layer thickness increases, is the AP configuration is difficult to achieve, especially at low temperatures, due to the strong demagnetization of FM interlayers caused by magnetization enhancement. Thus, both R_P and R_{AP} show a relatively weak temperature dependence, and the MR ratio increases only by a few percent when temperature decreases to 5 K (case iii).

The change in the MR ratio as the temperature decreases from 300 to 5 K is different for each case. Thus, ΔMR/MR(300 K) can be used to classify our samples, where the ΔMR is defined as MR(5 K) – MR(300 K). The ΔMR/MR(300 K) values as a function of interlayer thickness for Fe and Co are shown in Figs. 7(a) and 7(b). As the Fe thickness increases, ΔMR/MR(300 K) gradually decreases to around 1, which reveals that the tunneling process is gradually dominated by coherent tunneling. When the t_{Fe} further increases, ΔMR/MR(300 K) decreases to around 0.4 due to the strong demagnetization of Fe, which is case iii. The situation is different for Co. ΔMR/MR(300 K) increases for the samples with a thin Co interlayer ($t_{Co} \sim 0.5$ nm). This may be due to the magnetization frustration resulting from the AF coupling between MnGa and Co and/or relatively stronger element diffusion resulting from the additional *in situ* annealing after Co deposition. ΔMR/MR(300 K) stays at around 1 when the Co thickness is up to 1.5 nm. This implies that MnGa/Co is more stable than MnGa/Fe for maintenance of PMA due to the stronger exchange coupling for the MnGa/Co case.

Figures 6(a), 6(b), and 6(c) show the temperature dependence of the $R_{P,AP}$ for the samples with the core structures Mn$_{70}$Ga$_{30}$(30)/MgO(2.2)/CoFeB(1.2), Mn$_{62}$Ga$_{38}$(30)/Co (1.5)/MgO(2.2)/CoFeB(1.2), and Mn$_{62}$Ga$_{38}$(30)/Fe(1.1)/ MgO(2.2)/CoFeB(1.2), which are under the cases i, ii, and iii, respectively. The pink solid lines in each figure are the fitted
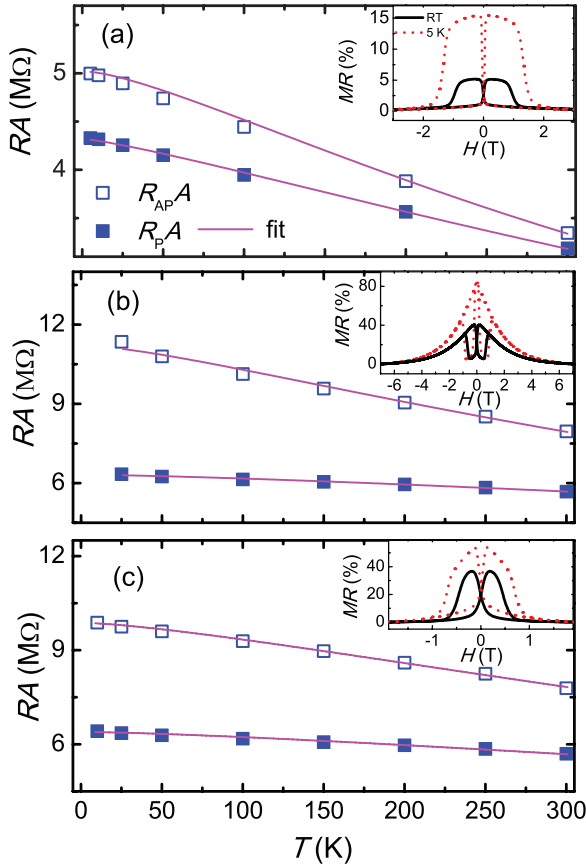
FIG. 6. (Color online) Temperature dependence of $R_{P,AP}$ of MTJs with the core structure (a) $Mn_{70}Ga_{30}(30)/MgO(2.2)/CoFeB(1.2)$, (b) $Mn_{62}Ga_{38}(30)/Co(1.5)/MgO(2.2)/CoFeB(1.2)$, and (c) $Mn_{62}Ga_{38}(30)/Fe(1.1)/MgO(2.2)/CoFeB(1.2)$. The square dots and the solid lines in the figure denote the experimental data and fit using formulas (4) and (5). The inset in each figure shows the $MR(H)$ curves at 300 K (black solid line) and 5 K (red dotted line).

results using formulas (4) and (5). The well fitting for all three samples indicates the model here can be used to describe our samples. The inset in each figure shows the $MR(H)$ curve at 300 and 5 K.

The fitted E_c and σ values are of interest, which reflect the extent of magnon and impurity assisted transport in the MTJs. The parameters E_c and σ can be obtained from the fitting. In order to compare the contribution of the hopping process for different samples, σ is normalized by the total G. The ratio of $\sigma/G_P(0,0)$ is used to evaluate the impurity effect.

The effects of the interlayer on E_c and $\sigma/G_P(0,0)$ are shown in Figs. 7(c)–7(f). For both the Fe and Co interlayers, as the thickness increases, E_c increases and $\sigma/G_P(0,0)$ decreases. This clearly reveals that the interlayer restrains inelastic transport from magnon excitation and impurity hopping. In addition, the increase in E_c and decrease in $\sigma/G_P(0,0)$ of the samples with Co interlayer are quantitatively larger than those for the Fe interlayer, as seen from Figs. 7(c), 7(e) and 7(d), 7(f). This indicates that Co is more effective in restraining the Mn impurity diffusion and magnon excitation.
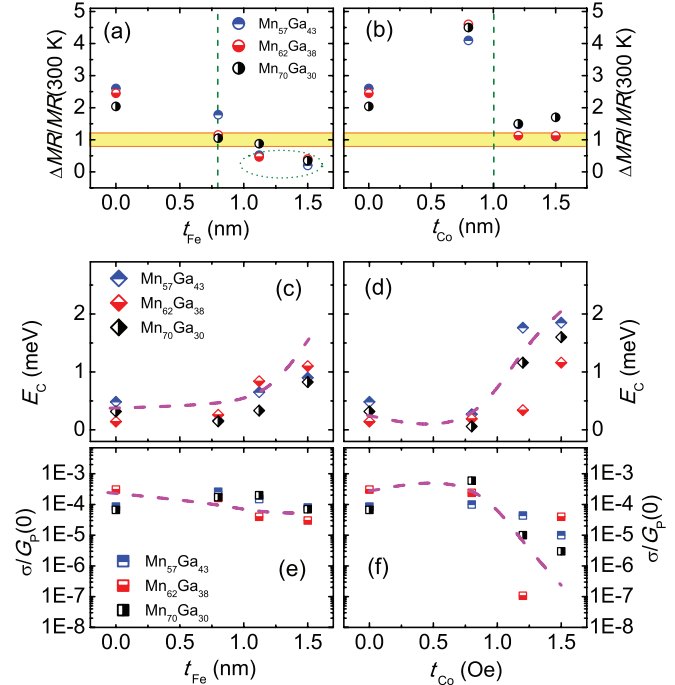

FIG. 7. (Color online) $\Delta MR/MR(300 K)$ as a function of interlayer thickness for (a) Fe interlayer and (b) Co interlayer. The area with $\Delta MR/MR(300 K)$ around 1 is marked in yellow shadow. E_c and $\sigma/G_P(0,0)$ as a function of interlayer thickness for Fe [(c) and (e)] and Co [(d) and (f)]. The dashed line is a guide to the eye.

VII. SUMMARY

In summary, we have characterized the structural and magnetic properties of the MnGa based p-MTJs and discussed in detail the dependence of the MnGa composition and interlayer thickness on the MR ratio of the MTJs with the core structure of MnGa/FM/MgO/CoFeB. In addition, the effect of the interlayer thickness on the transport properties is discussed based on the temperature dependence of the transport properties. The following conclusions can be drawn. (1) The magnetic properties and magnetoresistance effect reveal that the coupling for MnGa/Co and MnGa/Fe is different: Ferromagnetic and antiferromagnetic coupling are demonstrated for MnGa/Fe and MnGa/Co, respectively. (2) In MnGa/MgO/CoFeB p-MTJs, introduction of a thin FM layer causes the magnetoresistance ratio to increase significantly because of the interface optimization. An MR ratio of up to 50% is obtained at RT in MnGa based MTJs with a 1.5 nm FM interlayer. (3) The temperature dependence of the MR ratio in MTJs demonstrated that restraining of impurity induced hopping and magnon excitation would be the main reasons for the MR enhancement, and the Co interlayer is more effective in restraining the impurity diffusion and the magnon excitation.

ACKNOWLEDGMENTS

*Corresponding author: qinli-ma@wpi-aimr.tohoku.ac.jp

[1] B. Balke, G. H. Fecher, J. Winterlik, and C. Felser, Appl. Phys. Lett. **90**, 152504 (2007).

[2] F. Wu, S. Mizukami, D. Watanabe, H. Naganuma, M. Oogane, Y. Ando, and T. Miyazaki, Appl. Phys. Lett. **94**, 122503 (2009).

[3] S. Mizukami, T. Kubota, F. Wu, X. Zhang, T. Miyazaki, H. Naganuma, M. Oogane, A. Sakuma, and Y. Ando, Phys. Rev. B **85**, 014416 (2012).

[4] H. Kurt, K. Rode, M. Venkatesan, P. Stamenov, and J. M. D. Coey, Phys. Status Solidi B **248**, 2338 (2011).

[5] L. J. Zhu, S. H. Nie, K. K. Meng, D. Pang, J. H. Zhao, and H. Z. Zheng, Adv. Mater. **24**, 4547 (2012).

[6] J.-G. Zhu and C. Park, Mater. Today **9**, 36 (2006).

[7] J. A. Katine and E. E. Fullerton, J. Magn. Magn. Mater. **320**, 1217 (2008).

[8] S. Mizukami, F. Wu, A. Sakuma, J. Walowski, D. Watanabe, T. Kubota, X. Zhang, H. Naganuma, M. Oogane, Y. Ando, and T. Miyazaki, Phys. Rev. Lett. **106**, 117201 (2011).

[9] J. Winterlik, B. Balke, G. H. Fecher, C. Felser, M. C. M. Alves, F. Bernardi, and J. Morais, Phys. Rev. B **77**, 054406 (2008).

[10] Z. Bai, Y. Cai, L. Shen, M. Yang, V. Ko, G. Han, and Y. Feng, Appl. Phys. Lett. **100**, 022408 (2012).

[11] H. Kurt, K. Rode, M. Venkatesan, P. S. Stamenov, and J. M. D. Coey, Phys. Rev. B **83**, 020405(R) (2011).

[12] T. Kubota, S. Mizukami, D. Watanabe, F. Wu, X. Zhang, H. Naganuma, M. Oogane, Y. Ando, and T. Miyazaki, J. Appl. Phys. **110**, 013915 (2011).

[13] T. Kubota, M. Araidai, S. Mizukami, X. Zhang, Q. Ma, H. Naganuma, M. Oogane, Y. Ando, M. Tsukada, and T. Miyazaki, Appl. Phys. Lett. **99**, 192509 (2011).

[14] Q. L. Ma, T. Kubota, S. Mizukami, X. M. Zhang, H. Naganuma, M. Oogane, Y. Ando, and T. Miyazaki, Appl. Phys. Lett. **101**, 032402 (2012).

[15] K. Mizunuma, S. Ikeda, J. H. Park, H. Yamamoto, H. Gan, K. Miura, H. Hasegawa, J. Hayakawa, F. Matsukura, and H. Ohno, Appl. Phys. Lett. **95**, 232516 (2009).

[16] M. Nakayama, T. Kai, N. Shimomura, M. Amano, E. Kitagawa, T. Nagase, M. Yoshikawa, T. Kishi, S. Ikegawa, and H. Yoda, J. Appl. Phys. **103**, 07A710 (2008).

[17] M. Yoshikawa, E. Kitagawa, T. Nagase, T. Daibou, M. Nagamine, K. Nishiyama, T. Kishi, and H. Yoda, J. Appl. Phys. **44**, 2573 (2008).

[18] G. Lauhoff, C. Bruynseraede, J. De Boeck, W. Van Roy, J. A. C. Bland, and G. Borghs, Phys. Rev. Lett. **79**, 5290 (1997).

[19] W. L. O'Brien and B. P. Tonner, Phys. Rev. B **58**, 3191 (1998).

[20] J. Dresselhaus, D. Spanke, F. U. Hillebrecht, E. Kisker, G. van der Laan, J. B. Goedkoop, and N. B. Brookes, Phys. Rev. B **56**, 5461 (1997).

[21] T. Zhu, X. Xiang, F. Shen, Z. Zhang, G. Landry, D. V. Dimitrov, N. Garcia, and J. Q. Xiao, Phys. Rev. B **66**, 094423 (2002).

[22] Q. L. Ma, S. Iihama, T. Kubota, X. M. Zhang, S. Mizukami, Y. Ando, and T. Miyazaki, Appl. Phys. Lett. **101**, 122414 (2012).

[23] S. Yuasa, T. Nagahama, A. Fukushima, Y. Suzuki, and K. Ando, Nat. Mater. **3**, 868 (2004).

[24] J. Nogues, D. Lederman, T. J. Moran, and I. K. Schuller, Phys. Rev. Lett. **76**, 4624 (1996).

[25] J. M. Karanikas, R. Sooryakumar, G. A. Prinz, and B. T. Jonker, J. Appl. Phys. **69**, 6120 (1991).

[26] L. I. Glazman and K. A. Matveev, Zh. Eksp. Teor. Fiz. **94**, 332 (1988) [Sov. Phys. Semicond. **22**, 401 (1988)].

[27] Y. Lu, M. Tran, H. Jaffres, P. Seneor, C. Deranlot, F. Petroff, J. M. George, B. Lepine, S. Ababou, and G. Jezequel, Phys. Rev. Lett. **102**, 176801 (2009).

[28] C. H. Shang, J. Nowak, R. Jansen, and J. S. Moodera, Phys. Rev. B **58**, R2917 (1998).

[29] L. Yuan, S. H. Liou, and D. Wang, Phys. Rev. B **73**, 134403 (2006).

[30] S. G. Wang, R. C. C. Ward, G. X. Du, X. F. Han, C. Wang, and A. Kohn, Phys. Rev. B **78**, 180411(R) (2008).

[31] Q. L. Ma, S. G. Wang, J. Zhang, Y. Wang, R. C. C. Ward, C. Wang, A. Kohn, X.-G. Zhang, and X. F. Han, Appl. Phys. Lett. **95**, 052506 (2009).

[32] S. Zhang, P. M. Levy, A. C. Marley, and S. S. P. Parkin, Phys. Rev. Lett. **79**, 3744 (1997).

[33] V. Drewello, J. Schmalhorst, A. Thomas, and G. Reiss, Phys. Rev. B **77**, 014440 (2008).

[34] X.-F. Han, Andrew C. C. Yu, M. Oogane, J. Murai, T. Daibou, and T. Miyazaki, Phys. Rev. B **63**, 224404 (2001).

[35] J. Schmalhorst, A. Thomas, S. Kämmerer, O. Schebaum, D. Ebke, M. D. Sacher, G. Reiss, A. Hütten, A. Turchanin, A. Golzhauser, and E. Arenholz, Phys. Rev. B **75**, 014403 (2007).

[36] Y. Wang, Z. M. Zeng, X. F. Han, X. G. Zhang, X. C. Sun, and Z. Zhang, Phys. Rev. B **75**, 214424 (2007).